

AERODYNAMIC PERFORMANCE OF AN ACTIVE FLOW CONTROL CONFIGURATION USING UNSTRUCTURED-GRID RANS

Ronald D. Joslin
The Pennsylvania State University
PO Box 30, State College, PA 16804
and
Sally A. Viken
NASA Langley Research Center
Mail Stop 170, Hampton, VA 23681

1 Abstract

This research is focused on assessing the value of the Reynolds-Averaged Navier-Stokes (RANS) methodology for active flow control applications. An experimental flow control database exists for a TAU0015 airfoil, which is a modification of a NACA0015 airfoil. The airfoil has discontinuities at the leading edge due to the implementation of a fluidic actuator and aft of mid chord on the upper surface. This paper documents two- and three-dimensional computational results for the baseline wing configuration (no control) with the experimental results. The two-dimensional results suggest that the mid-chord discontinuity does not effect the aerodynamics of the wing and can be ignored for more efficient computations. The leading-edge discontinuity significantly affects the lift and drag; hence, the integrity of the leading-edge notch discontinuity must be maintained in the computations to achieve a good match with the experimental data. The three-dimensional integrated performance results are in good agreement with the experiments inspite of some convergence and grid resolution issues.

2 Introduction

Increased attention has been devoted to the development of techniques^{1,2} capable of enhancing our ability to control steady and unsteady flows in a wide variety of configurations and applications. Controlling the flow in and around these configurations can lead to improved efficiency and performance compared to uncontrolled configurations. While passive devices, such as the micro vortex generator^{3,4} have successfully been incorporated into production vehicles, passive devices are primarily limited to a single function or are effective over small operational ranges. Although decades of research

have been conducted using classical active controls (e.g., suction laminar flow control⁵), questions of system complexity and/or cost versus benefit have prevented such controls from reaching marketable applications. The recent invention of novel actuator concepts, some of which are locally applied and require only electrical power input, has introduced the potential for notably new vehicle control. Or, these new actuator/effector technologies may cause a paradigm shift in the design of conventional systems. Such a paradigm shift in high-lift system design for transport aircraft has led to a projected decrease in the weight, cost, and part-count of a conventional vehicle with flow control augmented high-lift systems.⁶ Such benefits are then compounded into fuel savings and emission and noise reductions.

A limited number of active flow control applications have been tested in the laboratory and in flight. These applications include dynamic stall control using a deformable leading edge,⁷ separation control for takeoff and landing flight conditions using piezo devices,^{8,9} pulsed vortex generators,¹⁰ and zero-net-mass oscillators,^{11–13} and thrust vectoring with piezo-driven oscillatory actuation.¹⁴

Laboratory and flight demonstrations of technology are essential to assess the technical feasibility of an innovative concept; however, accurate design and analysis tools can potentially lead to revolutionary new configurations and are a critical component in the estimation of the cost versus benefit of the technology on a real application. Hence, this paper will focus on the validation of design tools toward active flow control applications.

As yet, there is no definitive comparison with experimental data that indicates current computational capabilities can quantitatively predict the large aerodynamic performance gains achieved with active flow control in the laboratory. However, one

study¹⁵ using the RANS methodology has shown good quantitative agreement with experimental results for an isolated zero-net-mass actuator. In addition, some recent studies^{16–18} have used RANS to demonstrate qualitative performance gains compared with the experimental data for separation control on an airfoil. Quantitative comparisons for both baseline and flow control cases indicated that computational results were in poor quantitative agreement with the experiments.^{16,17}

The current research will investigate the potential use of an unstructured grid RANS approach to predict aerodynamic performance for active flow control applications building on the early studies.^{16,17} Before proceeding to the time-dependent flow control case, the computational results must quantitatively match experiments for the no control case. This paper compares the two- and three-dimensional simulation results with experiments for the baseline (no control) case.

The next section describes the configurations used for the computations and the experiments. The computational approach is then described followed by two- and three-dimensional results and concluding remarks.

3 Airfoil Configurations and Experimental Data

Figure 1 shows the leading edge and trailing edge regions of the configurations used in the present study. The mid-chord regions for all airfoils merge to the same configuration at 20% chord and therefore are not shown in figure 1. A NACA0015 airfoil is used in the study to provide reference point results. The blunt trailing edge of the NACA0015 airfoil matches the TAU0015. The TAU0015 airfoil model was tested in a low-speed wind tunnel at the Tel-Aviv University (TAU). The model is a NACA0015 airfoil modified in the leading-edge region to accommodate an actuation slot. Hence, the airfoil configuration is referred to as the TAU0015 airfoil. The TAU0015 model has a 0.3645 m chord, a 0.3% thick blunt trailing edge, and a 0.4% chord thick notch at 76.6% chord, which results from the flap/main element connection used in a different experiment. The actuator for the TAU0015 tests was located at the leading edge and leads to the 0.3% chord discontinuity (straight horizontal line region).

The previous two-dimensional computational studies^{16,17} used single-block structured grid RANS

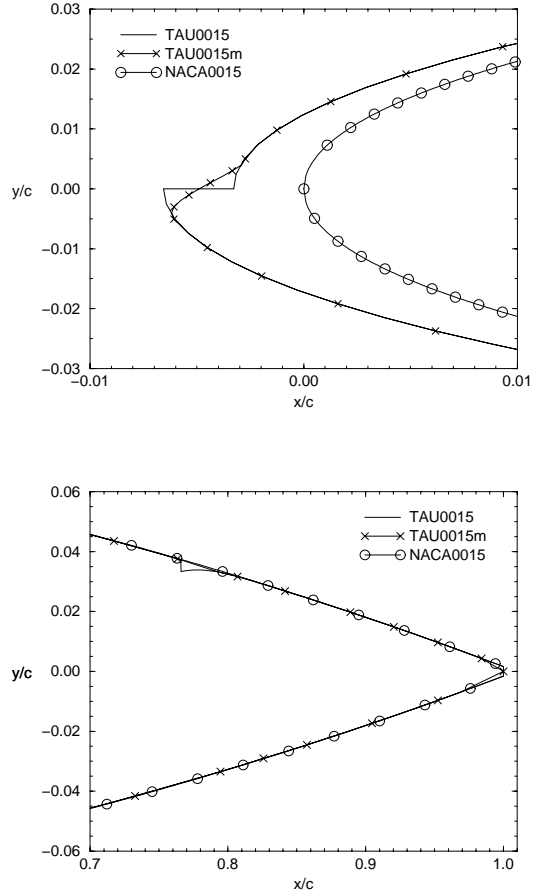


Figure 1: TAU0015, TAU0015m, and NACA0015 airfoils.

and for convenience ignored the 76.6% chord notch and trailing edge thickness and faired over (smoothed) the leading edge discontinuity. Here, this altered configuration is shown in figure 1 and is referred to as TAU0015m. Computational results for the TAU0015m will be compared with the TAU0015 configuration. There is no experimental data for the TAU0015m model.

The flow control experiments with the TAU0015 airfoil were conducted in the Meadow-Knapp Low Speed Wind Tunnel at the Tel Aviv University.¹¹ The test section is 1.50 m high and 0.61 m wide. The TAU0015 model was instrumented with 36 static pressure taps located on the model centerline and measurements were made sequentially using a multi-port, mechanical rotary valve (Scanivalve) and a 5 psi full scale differential pressure transducer. The transducer has an accuracy of 0.06% full scale. The free stream velocity of all tests was nominally 51 m/s. The pressure coefficient results are accurate to within $\pm 0.6\%$. Lift (C_l) and drag (C_d) coefficients are obtained by integrating the measured pressures; accuracy in C_l is estimated to be ± 0.01 for pre-stall conditions and ± 0.03 post-stall. The drag coefficient C_d has experimental uncertainty of ± 0.003 at pre-stall conditions and $\pm 10\%$ at post-stall conditions.¹⁹ The experimental conditions are at a Mach number of 0.15 and a chord Reynolds numbers of 1.2 million. The uncertainty in Reynolds number is $\pm 2\%$ due to variations in temperature and velocity during the tests.

The C_l and C_d for the experimental data is available at angle of attacks (α) from 0° to 24° in 2° increments. The maximum lift coefficient is $C_l=1.056$ at $\alpha = 12^\circ$. In addition, pressure coefficients (C_p) at $\alpha = 8^\circ$, $\alpha = 12^\circ$, $\alpha = 14^\circ$, and $\alpha = 22^\circ$ are used for the current comparison.

4 Computational Approach

The fully unstructured Navier Stokes two dimensional (FUN2D)²⁰ and three dimensional (FUN3D)²¹ codes solve the time dependent Reynolds-Averaged Navier-Stokes equations. The equations are expressed as a system of conservation laws relating the rate of change of mass, momentum, and energy in a control volume to the fluxes of these quantities through the control volume. The solver is an implicit, upwind-differencing algorithm with the inviscid fluxes obtained on each face of the control volume, employing Roe's flux-

difference-splitting scheme. The node-based algorithm stores the variables at the vertices of the mesh and the equations are solved on the non-overlapping control volumes surrounding each node. The viscous terms are discretized using a central-difference formulation. Time-advancement is made with a linearized backward Euler scheme. At each time step, the equations are solved with 15 Gauss-Seidel sub-iterations, sequentially solving for all odd numbered nodes and then all even numbered nodes. A two-level V-type multigrid approach is used for the two-dimensional baseline study to accelerate convergence.²¹ No multigrid acceleration was used for the three-dimensional calculations. A very fine grid was first used to determine the affect of the geometric discontinuities on the aerodynamic performance. Grid coarsening was implemented to improve computational efficiency without sacrificing accuracy. The Spalart-Allmaras turbulence model²² is used in this investigation and all computations assume fully turbulent flow. A single-processor SGI OCTANE was used for the two-dimensional computations. The three-dimensional calculations were conducted on a SGI ORIGIN 2000 machine using 8 processors.

The two-dimensional unstructured grids were generated with advancing front type point placement with iterative local re-meshing for grid quality improvement.^{23,24} Figure 2 shows an initial coarse grid around the TAU0015 airfoil, resolving all discontinuities on the configuration. Similar grids were generated for the TAU0015m and NACA0015 airfoils. The grids extend from the airfoils to form a far-field circle with a radius of 20 chord lengths around the airfoils.

The three-dimensional simulations were conducted on the TAU0015 to validate the computational approach with the experiments. Future active flow control simulations will involve the use of fully three-dimensional actuation technologies and therefore a validation of the three-dimensional code on the baseline (no control) cases is essential.

The three-dimensional TAU0015 grids were obtained using the TetrUSS unstructured grid package.²⁵⁻²⁷ The grid generation technique is based on the Advancing-Front (AFM) and the Advancing-Layers (ALM) methods and produce fully tetrahedral meshes. In defining the computational domain, boundaries are represented by bilinear surface patches. The patches are defined only in terms of their edges, which are constructed in GRIDTOOL based on user-specified geometries.

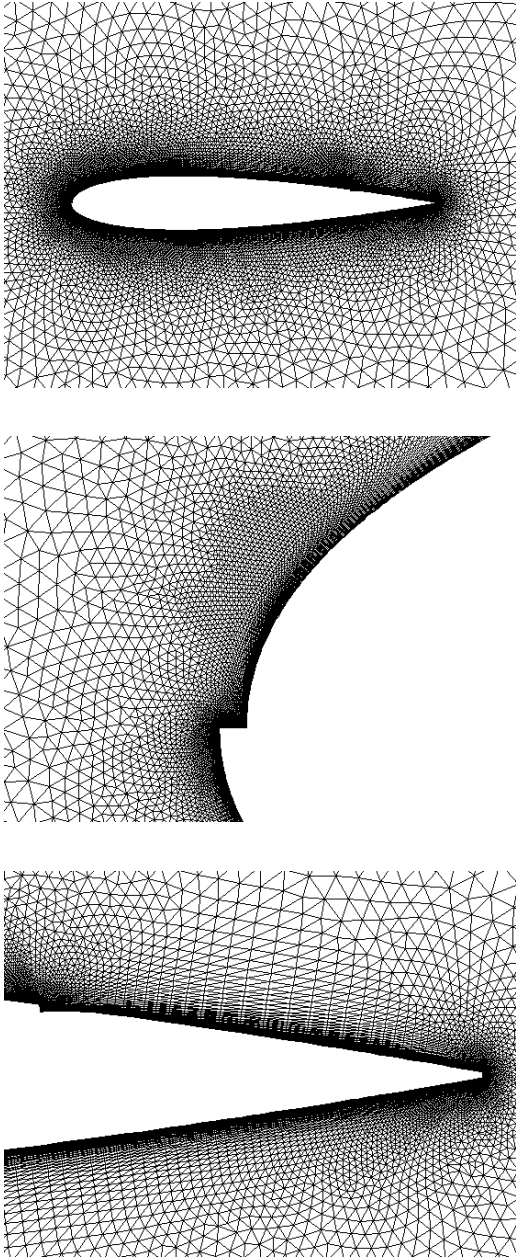


Figure 2: Two-dimensional grid for TAU0015 airfoil (top), leading edge region (middle), and aft portion of wing (bottom).

Grid characteristics such as cell spacing and stretching are also specified in GRIDTOOL by the placement of cell "sources". The surface mesh is generated in VGRID by triangulating each surface patch with a two-dimensional version of the advancing-front method. The triangulated surface patches then form the initial "front" for the advancement of the three-dimensional tetrahedral volume cells. The high aspect ratio cells in the viscous region are constructed with the ALM, where individual cells are formed by inserting a point based on surface vector information. Finally, the isotropic cells were constructed in the inviscid region using the AFM. Smooth propagation of grid spacing is achieved by solving a Poisson equation on a cartesian background grid, using the GRIDTOOL defined cell sources as inputs. Once the volume grid is generated, local remeshing can be implemented for grid quality improvements.

The three-dimensional TAU0015 surface grid has a spanwise length of approximately one chord length. The outer boundary of the grid extends 10 chord lengths out from the airfoil geometry forming a box. Figure 3 shows the surface grid at the leading edge of the TAU0015 airfoil. The cells are clustered near the leading edge step region to resolve the geometry and capture the flow field characteristics at this discontinuity. The volume grid has 1.85 million cells. The sidewalls of the computational domain were treated as inviscid walls, with the remaining outer boundaries treated as characteristic inflow/outflow surfaces. No-slip viscous boundary conditions were prescribed on the airfoil surface. A more thorough discussion of the three-dimensional grids will be provided in the three-dimensional results section.

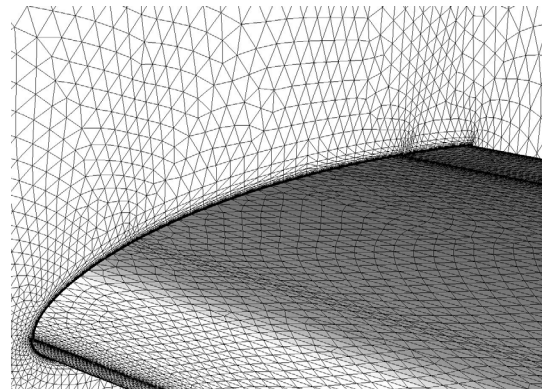


Figure 3: Three-dimensional surface grid for TAU0015 airfoil.

Case	Grid1 Total Nodes	Grid1 Surface Nodes	Grid2 Total Nodes	Grid2 Surface Nodes
(a)	114119	1891	51150	1260
(b)	48063	1032	21316	516
(c)	62764	1100	25352	550

Table 1: Number of nodes used for (a) TAU0015, (b) TAU0015m, and (c) NACA0015 airfoils.

5 Two-Dimensional Results

In this section, the fine-grid two-dimensional computational results are compared with experiments. A grid de-refinement analysis is then conducted to minimize the number of required grid points. The de-refinement analysis is necessary to minimize the cost of the three-dimensional computations.

5.1 Fine Grid Comparison with Experiments

All grids in the initial computations had the first near-surface grid point below $y^+ = 0.7$ to ensure the sublayer of the turbulent shear flow was sufficiently resolved. Specification of the first grid point approximation is based on relationships among y^+ , Reynolds number, and the skin-friction for a flat plate boundary layer. For turbulent flow, this relationship is $y^+ = \Delta y \cdot \sqrt{c_f/2Re}$, where $c_f \simeq 0.455/\ln^2(0.06Re_x)$ and Δy is the physical distance for the first grid point away from the airfoil surface. Specifying a midchord $y^+ = 0.102$ will keep all near-wall points below 0.7 as will be shown later.

The number of surface nodes and total grid nodes for the first comparison are shown in Table 1 for each airfoil. The TAU0015 airfoil grid has significantly more grid points because of the grid clustering near the surface discontinuities, which are not present in the TAU0015m and NACA0015 airfoils.

Convergence of the steady-flow computations were achieved when the change in C_l was less than 0.015% per iteration. At this criteria, C_d changed by less than 0.005% per iteration. The only unsteadiness in the computations was observed at $\alpha = 26^\circ$ where unsteady vortex shedding was evident.

Figure 4 shows the computed C_l with variation in α for the NACA0015, TAU0015, and TAU0015m airfoils compared with the experimental data. For

the NACA0015, the maximum lift coefficient, C_l , and stall angle, α , are 30% and 4° higher than the experimental data. For the TAU0015m airfoil, the maximum C_l and stall angle are 23% and 2° higher than the experiments. Overpredictions for the TAU0015m airfoil are consistent with the earlier studies^{16,17} which used the same airfoil but a structured grid and two different RANS codes. In closer agreement, the computed results for the TAU0015 airfoil approach the experimental results. The stall angle is overestimated by 1° and the maximum C_l by 15%. The subtle differences in geometry for the NACA0015, TAU0015m and TAU0015 airfoils lead to large differences in the computed stall angle α and maximum C_l . The drag coefficient comparison indicates that all computations overpredict drag prior to stall and underpredict drag in post-stall conditions. However, the TAU0015 results are in better agreement with the experiments than the NACA0015 and TAU0015m results.

A reasonable explanation for the differences between the computational and experimental results for the TAU0015 geometry may be obtained with a careful review of the experimental results. In the experiments, C_l and C_d are derived from numerical integration of the static pressure measurements at discrete locations, whereas the computations used pressure around the complete airfoil and included viscous drag contributions. Hence, a comparison of computed and measured pressure information is necessary for this review. Figure 5 shows computed pressure coefficients (C_p) for the TAU0015 airfoil compared with experimental results for $\alpha = 8^\circ$ and $\alpha = 12^\circ$ (pre-stall) and 22° (post-stall). The computational results show pressure spikes at the leading edge and near 76% chord resulting from the geometrical discontinuities. Pressure spikes were not measured in the wind-tunnel experiments because taps could not be positioned on the actuator. Therefore, the experiments could not capture the additional pressure spikes predicted in the computations.

Based on this understanding of the experimental data, C_l and C_d were recomputed by integrating the pressure over the TAU0015 airfoil in regions consistent with the experimental pressure taps. That is, the contribution from the leading-edge actuator discontinuity is now excluded in the determination of C_l and C_d . The new C_l and C_d variation with α are compared with experimental data in figure 6. The computed maximum C_l is now overpredicted by 2% compared with the experimental data and the stall angles of attack are in agreement at 12° . The

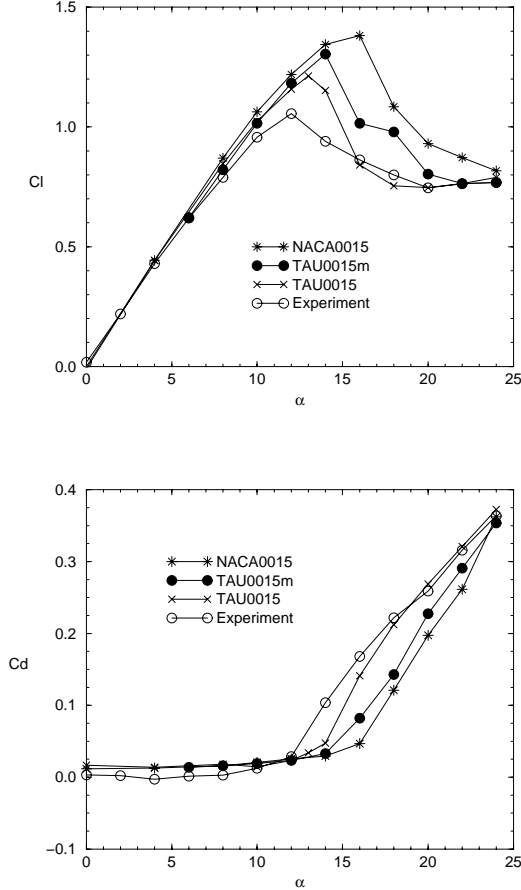


Figure 4: Lift (C_l) and drag (C_d) coefficients versus angle-of-attack (α) for experiments compared with computations for TAU0015, TAU0015m, and NACA0015 airfoils.

overprediction in lift results in an underprediction of the drag. The post-stall (separated) conditions show notable disagreement between computational and experimental results.

Because the SA turbulence model was not developed or validated for separated flows, significant uncertainty exists in the computations for post-stall cases. Further, there is notable experimental uncertainty for post-stall conditions as confirmed in results for a simple NACA0012 airfoil.^{28,29} Hence, the computational and experimental results each have uncertainty in their respective quantities for highly separated flow conditions.

5.2 Coarse Grid Solutions

In any grid generation process, judgment must be made concerning the adequacy of the grids for the computations. This is usually accomplished by grid refinement studies. For the current study, the alternate approach of excessive grid refinement was used to obtain a solution that matches the experimental results. This approach allows assessment of confidence in the RANS methodology. To achieve the current grid for the TAU0015 airfoil, extensive grid clustering near the discontinuities was used to resolve any possible regions of flow re-circulation. In this section, the process of grid coarsening is discussed.

Table 2 shows the number of surface nodes and total nodes for various grid coarsening strategies. The first row in Table 2 is the fine grid TAU0015 configuration shown as the first item in Table 1. The *No Cluster* case shows a decrease in the number of nodes by removing the grid clustering at the leading-edge, 76% chord, and the trailing edge. The *No Cluster/Notch* case combines removal of discontinuity grid clustering and removal of the notch geometry at 76% chord. *Coarse Grid 1* reduces the total number of surface nodes relative to the *No Cluster/Notch* case by approximately 2. *Coarse Grid 2* reduces the number of surface nodes on the actuator and lower surface of the airfoil by approximately 2 compared with the *No Cluster/Notch* case. The finer grid on the upper surface is retained, however, so the separation point can be more accurately computed.

Figure 7 shows lift and drag coefficients for the grid de-refinement cases compared with the original TAU0015 results. The coarse-grid results are sufficiently close to the TAU0015 experimental results (within experimental uncertainty levels) and

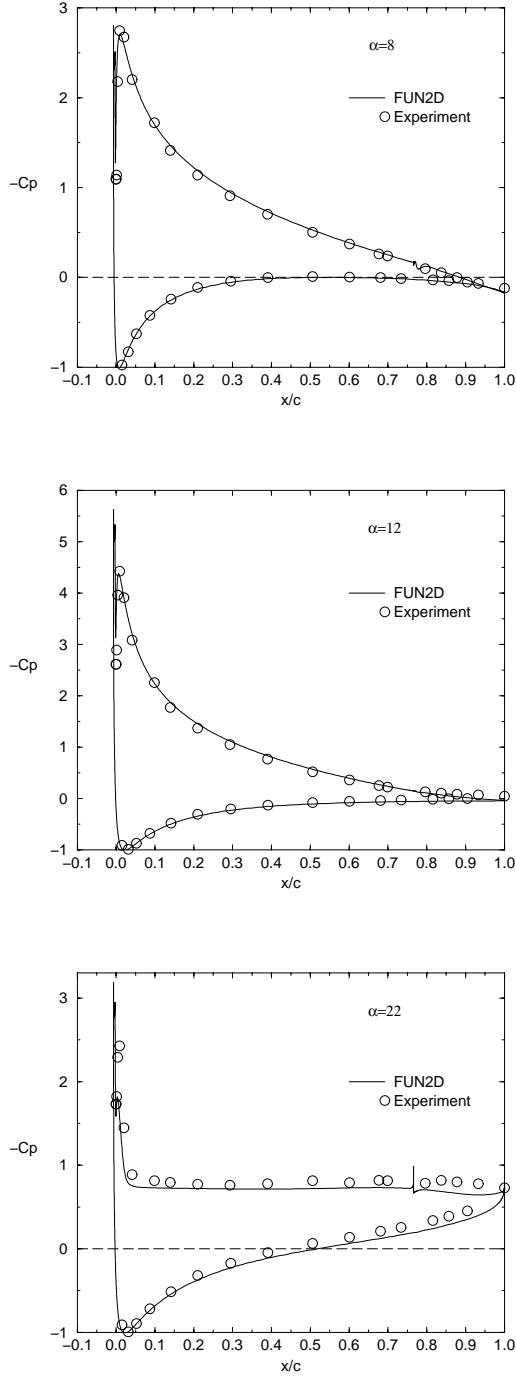


Figure 5: Computational and experimental pressure coefficients (C_p) for TAU0015 airfoil at $\alpha = 8^\circ$ and $\alpha = 12^\circ$ (pre-stall) and $\alpha = 22^\circ$ (post-stall) for TAU0015 airfoil.

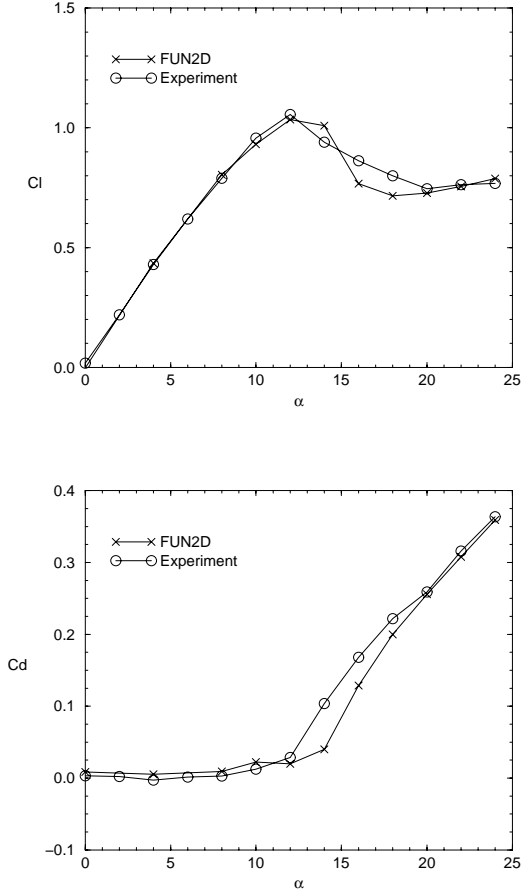


Figure 6: Lift (C_l) and drag (C_d) coefficients versus angle-of-attack (α) for computations and experiments for TAU0015 airfoil.

Case	Grid1 Total Nodes	Grid1 Surface Nodes	Grid2 Total Nodes	Grid2 Surface Nodes
(a)	114119	1891	51150	1260
(b)	69331	1480	30401	712
(c)	68103	1406	30040	716
(d)	36988	716	16439	346
(e)	47965	936	21770	482

Table 2: Number of nodes used for (a) TAU0015, (b) No Cluster, and (c) No Cluster/Notch cases, (d) Coarse Grid 1, and (e) Coarse Grid 2 cases.

Case	C_l	%Error
(a)	1.056	
(b)	1.034	2.1
(c)	1.030	2.4

Table 3: Lift coefficient (C_l) for (a) Experiment, (b) TAU0015, and (c) *Coarse Grid 2* cases at $\alpha = 12^\circ$. (Computational error relative to experiment)

avoid the added expense of including the notch and grid clustering in the computations. Comparing the *Coarse Grid 1* and *Coarse Grid 2* results indicates that significant grid coarsening can be used on the lower surface, but additional coarsening on the upper surface is not acceptable. Sufficient resolution on the upper surface is necessary to accurately compute the separation location.

Results for the *Coarse Grid 2* case are presented in a manner similar to that for the analysis leading to figure 6. The lift coefficient is recomputed for the *Coarse Grid 2* case without the pressure contribution from the actuation region at the leading edge. Table 3 shows the TAU0015 and *Coarse Grid 2* solutions along with the experimental result at $\alpha = 12^\circ$. (measurement station near maximum lift conditions). Over 65,000 points have been removed in the grid de-refinement process and the error in solution is approximately 2.4%.

For the final series of two-dimensional computations in this section, the effect of wall-normal grid resolution is examined to further minimize the required number of nodes necessary for an accurate solution. In section 5.1, it was noted that in all previous grids, the first grid point was well below $y^+ = 0.7$ to ensure sufficient resolution of the sub-layer of the turbulent boundary layer. The spacings

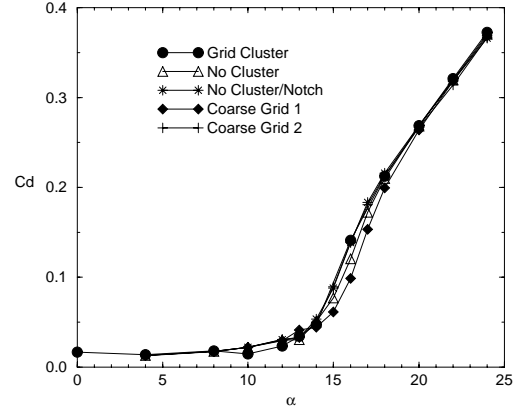
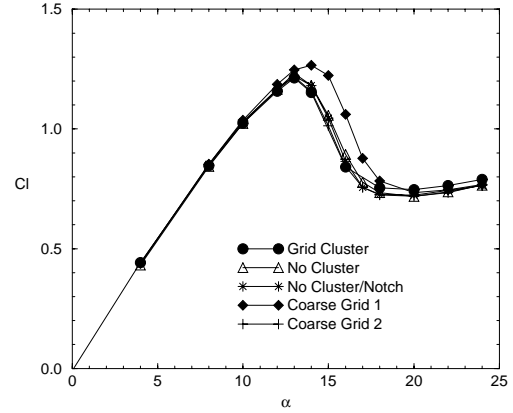


Figure 7: Lift (C_l) and drag (C_d) with angle of attack for the de-refinement cases.

y^+	Grid1 Total Nodes	Grid1 Surface Nodes	Grid2 Total Nodes	Grid2 Surface Nodes
0.102	47965	936	21770	482
0.700	36590	912	15573	456
1.382	33455	912	13831	456
7.000	27409	912	10442	456

Table 4: Number of nodes used for wall-normal grid coarsening.

for the final series of simulations are shown in Table 4. The resulting number of surface and total grid nodes are shown that result from increasing the distance between the airfoil and the first wall-normal grid point.

Figure 8 shows wall-normal grid coarsened lift and drag coefficients compared with the fine grid case. These results indicate additional grid coarsening can be achieved in the wall normal direction; however, as expected, the viscous region can become under-resolved and the results begin to lose accuracy. Again, the initial spacing of the first wall-normal grid point is approximated using the flat-plate turbulent boundary layer relationship discussed in section 5.1. However, a correlation for skin friction for airfoils does not exist to enable a determination of y^+ . For the cases in Table 4 that show relatively good quantitative agreement with the fine grid results, figure 9 shows the computed y^+ around the airfoil for $\alpha = 12^\circ$. The skin-friction varies with chordwise location (and α), therefore, y^+ varies with chordwise location. For these variations in y^+ , sufficient resolution overall is apparent with the good quantitative agreement in the results.

5.3 Three-Dimensional Results

In this section, three-dimensional pre-stall, stall, and post-stall flow conditions are investigated as a precursor to the active flow control simulations which will involve three dimensionality associated with actuator-induced flow fields.

Ideally, the three-dimensional calculations should encompass viscous boundary conditions associated with the wind tunnel walls; however, such computations are at this point prohibitively expensive. So initially inviscid walls with a subset of the wind tunnel domain are used for this first comparison of the three-dimensional computational results with

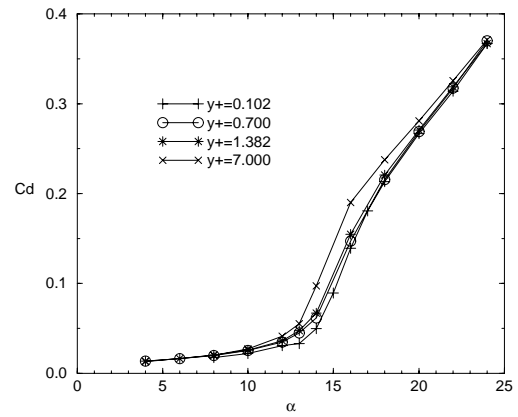
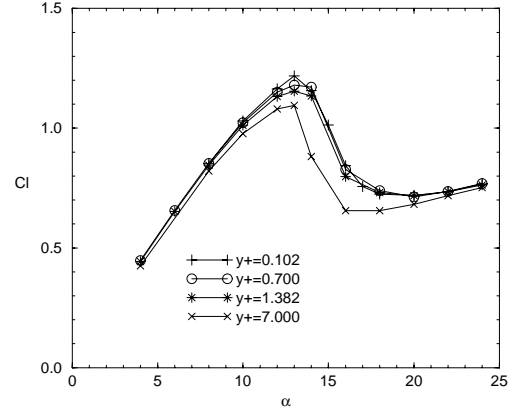


Figure 8: Lift (C_l) and drag (C_d) coefficients versus α for various near-wall initial grid spacing for TAU0015 airfoil.

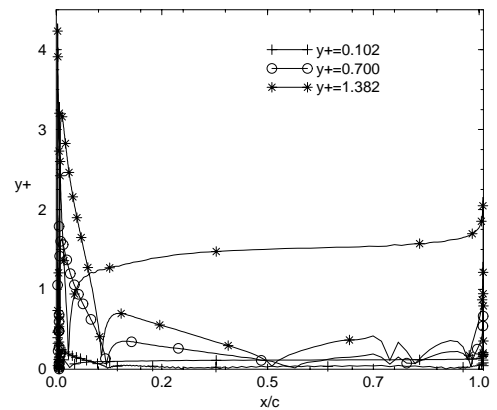


Figure 9: Computed y^+ with chordwise location for TAU0015 airfoil ($\alpha = 16^\circ$).

the two-dimensional simulation results and experimental data. Initial calculations were conducted in a volume grid that had a spanwise width equal to the airfoil chord. The outer boundary of the grid extended 10 chord lengths out from the airfoil geometry. Figure 3 shows the surface mesh at the leading edge of the TAU0015 airfoil. This surface grid maintained the discontinuity at 76% chord. The minimum normal wall spacing on the airfoil was determined based on a $y^+ = 0.7$, chord Reynolds number of 1.2 million, and the skin friction for a flat plate boundary layer. This grid had up to 26 layers of thin tetrahedral cells in the viscous region for the boundary layer with approximately 375 nodes along a chordwise surface cut. The total cell count for this volume grid was 1.85 million. Because the computational results with this grid did not match the two-dimensional results or the experimental data, the grid was regenerated around TAU0015 airfoil with a much finer grid.

As shown in figure 7 for the two-dimensional investigation, grid resolution on the upper surface was necessary to capture the separation location and to accurately predict integrated aerodynamic performance. For the three-dimensional "fine" grid, the stretching in the viscous layer was modified to obtain up to 33 layers of thin tetrahedral cells for the boundary layer with approximately 800 nodes along a chordwise surface cut. With the increase in grid density, the span of the grid was reduced from 1.0 to 0.5 chord lengths, resulting in a total cell count of 2.9 million. The surface discontinuity at 76% chord was omitted for this three-dimensional grid because the two-dimensional results demonstrated that this discontinuity does not effect the aerodynamics of the wing and can be ignored for more efficient computations. Figure 10 shows the surface mesh at the leading edge of the refined TAU0015 grid.

Three-dimensional computational flow analyses were conducted on the TAU0015 for a Mach number of 0.15 and chord Reynolds number of 1.2 million. The angles of attack analyzed were 8° , 10° , 12° , 14° , and 22° .

Convergence for the three-dimensional calculations was determined by two methods. The first method involved tracking the solution residual until it dropped several orders in magnitude and started to level out. For the second method, the C_l and C_d were monitored to verify that the solution had converged to a constant. The C_p distributions were evaluated at the final solution and at 1000 iterations prior to the final solution to ensure they were not

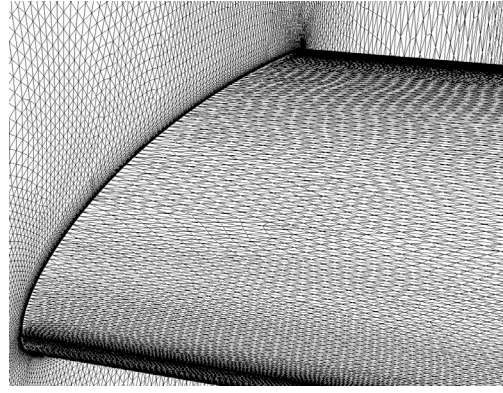


Figure 10: Three-dimensional fine grid case for TAU0015 airfoil.

changing. Figure 11 shows the convergence history plots for the $\alpha = 8^\circ$ case. The residual is reduced approximately 6 orders in magnitude and a near-constant lift coefficient is obtained in approximately 2000 iterations. Convergence for these steady flow computations is considered attained when C_l and C_d changed less than 0.5% and 0.3%, respectively, over the final 1000 iterations. All the cases required between 3000 and 6000 iterations to achieve this convergence criteria, except for the $\alpha = 14^\circ$ case which will be discussed later in this section.

The variation of three-dimensional computed lift (C_l) and drag (C_d) coefficients with angle of attack (α) for the TAU0015 airfoil are compared with the experimental data in figure 12. Both the coarse and fine grid three-dimensional computed results are shown. Here, the computed C_l and C_d are obtained by integrating the pressure distribution on the centerline of the model. The three-dimensional fine grid results are in better agreement with the experimental data compared with the coarse grid results, which are under-resolved. Further discussion will involve only the fine grid three-dimensional results.

For low- α pre-stall conditions ($\alpha < 8^\circ$), the three-dimensional C_l and C_d results are slightly greater than the experimental results. At the higher- α , pre-stall region ($\alpha \simeq 10^\circ$), the three-dimensional C_l and C_d results begin to more closely match the experimental results. Near stall angle conditions $\alpha = 12^\circ$, the computational results underestimates the maximum C_l by 3% but matches the stall angle. For post-stall conditions ($\alpha = 14^\circ$), the computed C_l deviates from the experimental data; however, the computed C_d closely follows the trends of the experimental data. With the separation bubbles on

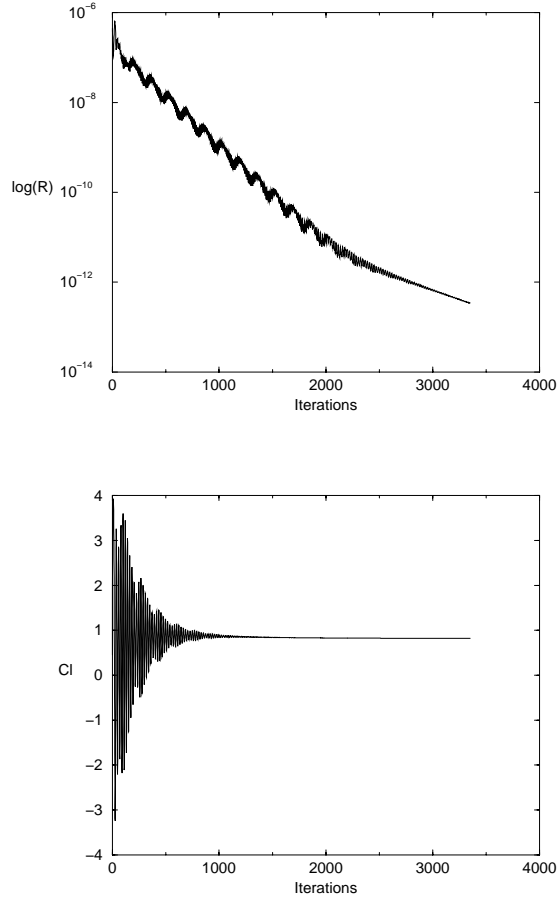


Figure 11: Convergence of residual and lift coefficient (C_l) with iteration for TAU0015 airfoil ($\alpha = 8^\circ$).

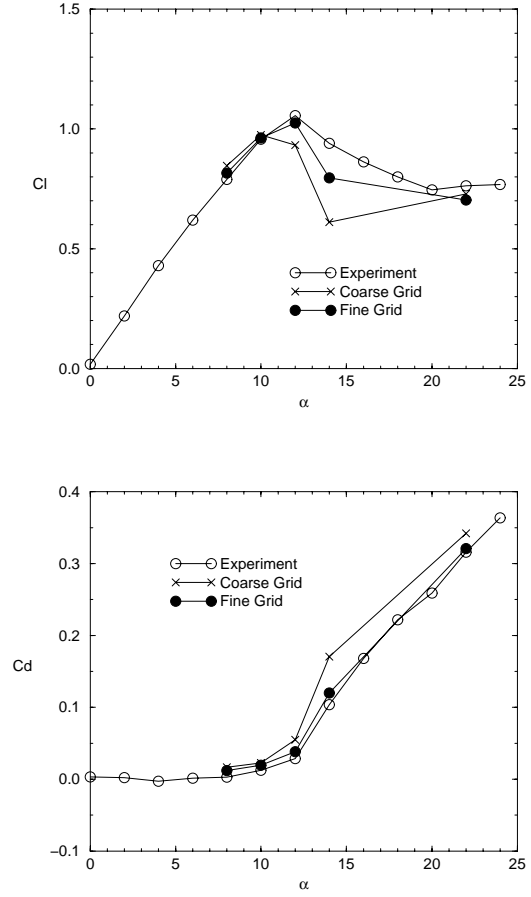


Figure 12: Lift (C_l) and drag (C_d) coefficients versus angle-of-attack (α) for experiments compared with three-dimensional computations for TAU0015 airfoil.

the upper surface becoming more developed at stall and fully separated flow at post-stall conditions, it is likely that the three-dimensional results are insufficiently grid-resolved to capture the true flow characteristics and quantitatively match experiments. A second plausible reason for the near-stall and post-stall disagreement in the results resides with deficiencies in the turbulence model. The model was developed for attached and steady flows.

Figure 13 shows the two- and three-dimensional computed pressure coefficients (C_p) compared with the experimental data for $\alpha = 8^\circ$. Overall, very good agreement is achieved at this pre-stall angle of attack. Analysis of the three-dimensional computational results show the flow accelerating from the stagnation point around the leading edge region of the airfoil and separating from the surface due to the backward facing step. The flow then reattaches at $x/c = -0.002$ followed by an accelerated flow region to x/c of approximately 0.01. The flow then negotiates the increasing pressure gradient at $x/c = 0.947$ before separating at the trailing edge. Note, that the three-dimensional computational pressure results overpredict both the two-dimensional and experimental data near the leading edge region.

Figure 14 represents a Mach contour map along the centerline of the three-dimensional grid for $\alpha = 12^\circ$ with the flow separation region visible. The two and three-dimensional computed pressure coefficients are compared with the experimental data in figure 15. The three-dimensional results show the flow separating in the leading edge actuator region, with reattachment at $x/c = -0.002$ and a slight flow acceleration region existing back to $x/c = 0.006$. The flow then negotiates the steep increasing pressure gradient back to $x/c = 0.535$ before flow separation occurs back to the trailing edge. The calculated pressure rise from the three-dimensional results is just slightly steeper than the two-dimensional results and the experimental data. Similar to the $\alpha = 8^\circ$ case, the three-dimensional pressures are overpredicted compared with the two-dimensional and experimental data.

Considerable effort has been expended on the post-stall case of $\alpha = 14^\circ$. In order to capture true flow physics for this case, the original coarse surface mesh cell spacing was reduced along with increasing the number of cells in the boundary layer of the grid. Neither the coarse nor the fine grid solutions were successful in matching the experimental aerodynamic performance of the TAU0015 for

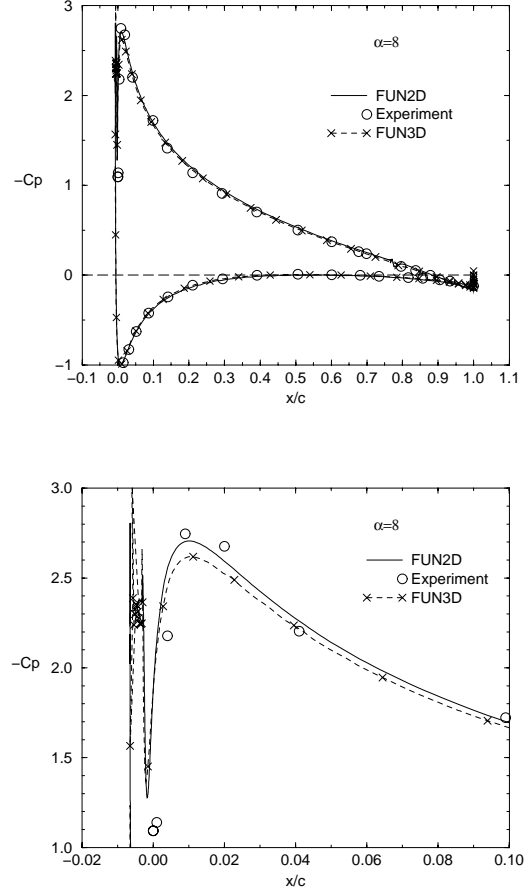


Figure 13: Two- and three-dimensional computational pressure coefficients (C_p) compared with experimental results for TAU0015 airfoil at $\alpha = 8^\circ$.

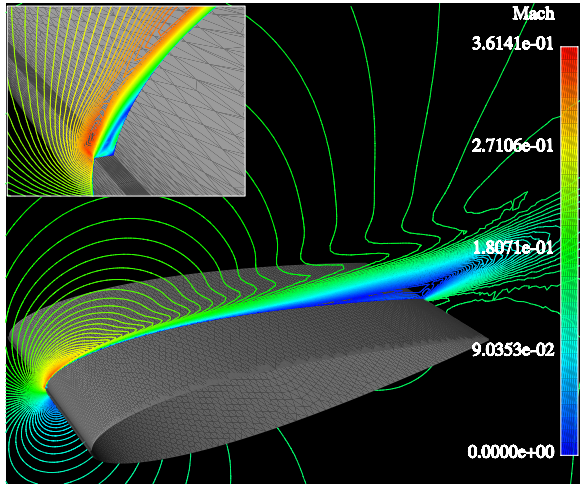


Figure 14: Mach contour map at centerline cut for TAU0015 airfoil at $\alpha = 12^\circ$ (insert of leading edge region).

this angle of attack. The fine grid case was halted after 11650 iterations before the convergence criterion was met due to the slow but steady decrease in C_l . The C_l at this point was 0.796. Examining the solution files showed the separation line progressing forward along the upper surface. Figure 16 shows the two- and three-dimensional computed pressure coefficient (C_p) for $\alpha = 14^\circ$ compared with experiments. Clearly, the difference between the two- and three-dimensional results has increased for the post-stall conditions. However, in this comparison, the three-dimensional results are in much better agreement with the experimental data over most of the airfoil.

The nearly converged surface pressure distribution (after 11650 iterations) along with particle traces on the upper surface are shown in figure 17 for $\alpha = 14^\circ$. A distortion is observed in the separation front (spanwise curvature near leading edge). The particles traces from the leading edge run parallel to the flow field until the separation line is approached. A spanwise bias to the separation front is observed symmetrically on both sides of the airfoil centerline. In the reverse flow region, the particles traces move from just ahead of the trailing edge ($x/c=.98$) up to the separation line and again turn outward toward the walls. It may be that the inviscid boundary conditions are adversely impacting the flow such that the inviscid-side-wall/leading-edge-juncture is causing a spanwise bias to separation front. Similar results were also found with the coarse grid solution. This behavior is not typical of inviscid boundary

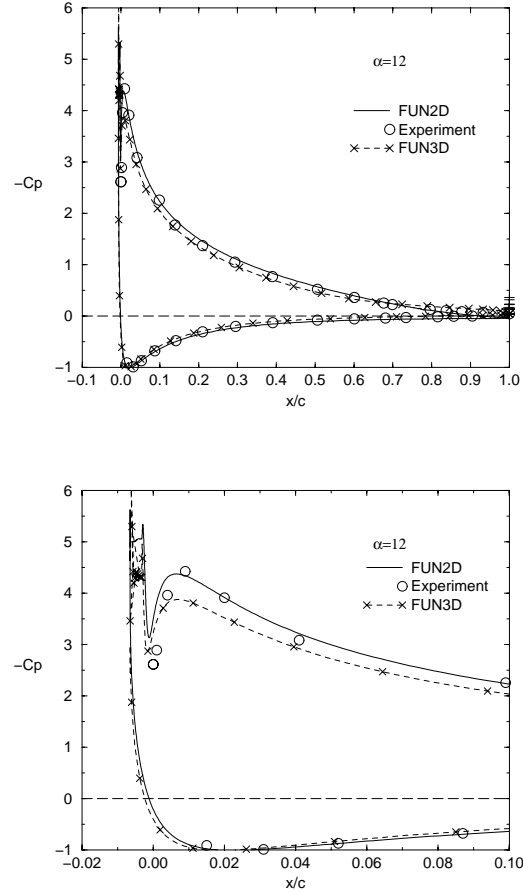


Figure 15: Two- and three-dimensional computational pressure coefficients (C_p) compared with experimental results for TAU0015 airfoil at $\alpha = 12^\circ$. (lower graph is expansion of leading edge region)

conditions and remains to be resolved.

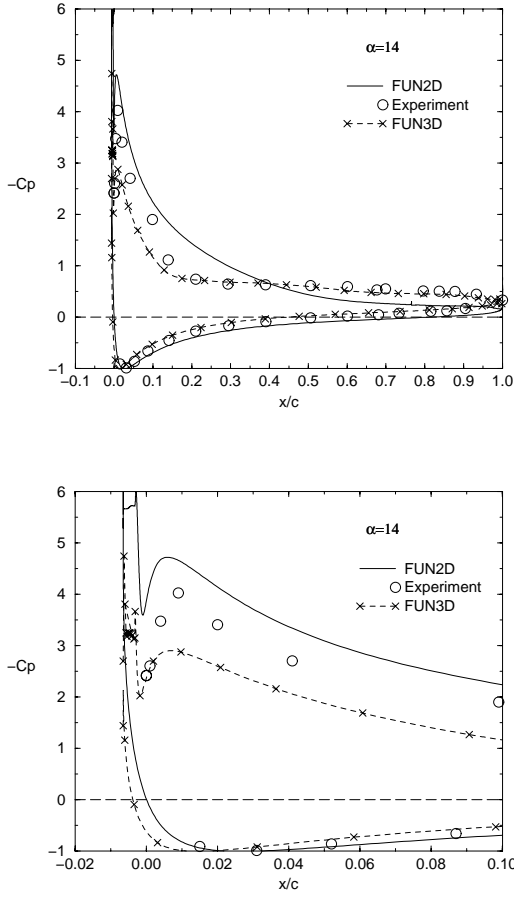


Figure 16: Two- and three-dimensional computational pressure coefficients (C_p) for TAU0015 airfoil at $\alpha = 14^\circ$. (lower graph is expansion of leading edge region)

Finally, figure 18 shows the two and three-dimensional computed pressure coefficients (C_p) compared with the experimental data for $\alpha = 22^\circ$. Reasonably good agreement is also achieved at this post-stall angle of attack over most of the airfoil. Three-dimensional computational results show the flow separating at the leading edge step with a small reattachment region from $x/c = -0.001$ to $x/c = 0.007$, followed by a massive flow separation region back to the trailing edge. Both two- and three-dimensional result overpredict the pressure near the leading edge for this extremely stalled case. The flow separation can be visualized in figure 19, with the Mach contour map along the centerline of the surface grid. Results

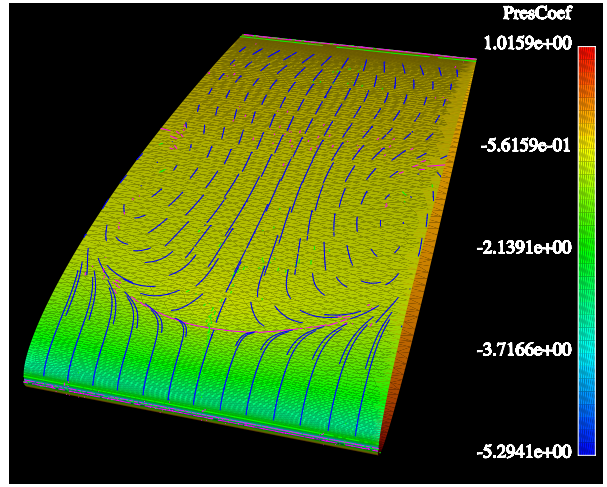


Figure 17: Three-dimensional surface pressure coefficient along with particle traces for TAU0015 airfoil at $\alpha = 14^\circ$.

from the three-dimensional calculations, however, did not capture the small flow acceleration region back to $x/c \simeq 0.01$ as found in the experiment.

In the analysis presented in figure 6 for the two-dimensional comparison with experiments, removing the contribution associated with the leading-edge actuator and re-integrating the pressures to obtain C_l and C_d lead to good agreement between computational and experimental results. If the actuator region is excluded from the integration in the three-dimensional analysis, the lift and drag decrease (as expected). For $\alpha = 12^\circ$, the lift coefficient C_l decreases by only 1.1% while the drag coefficient decreases by 8.1%. As such, the computed drag coefficient is in better agreement with the experimental results when the actuator region is neglected. Also, the secondary leading-edge pressure spike over the actuator region in the three-dimensional computations is smaller than in the two-dimensional computations; therefore, the change in C_l is smaller in the three-dimensional analysis compared with the two-dimensional analysis.

6 Conclusions

Results from two- and three-dimensional unstructured grid Reynold-Averaged Navier-Stokes codes were compared against an experimental database for a NACA0015 airfoil modified at the leading edge to implement a fluidic actuator. This actuator caused a discontinuity at the leading edge. This paper doc-

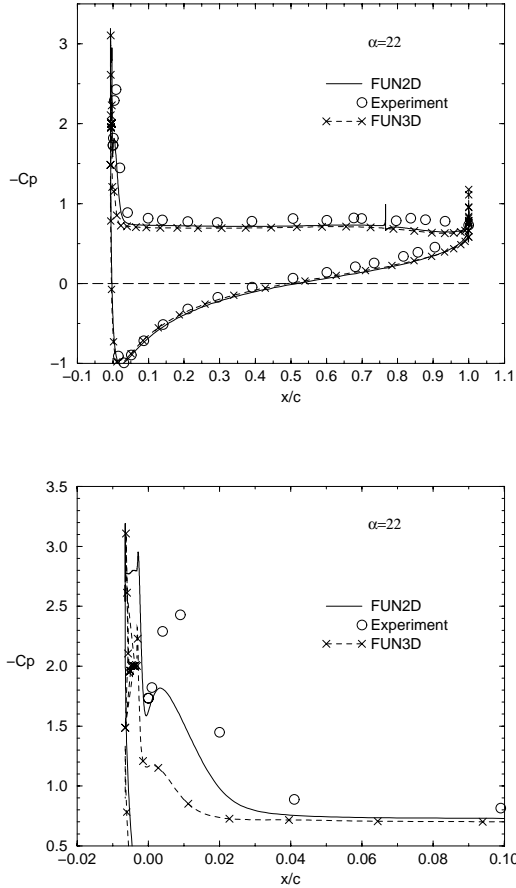


Figure 18: Two- and three-dimensional computational pressure coefficients (C_p) compared with experimental results for TAU0015 airfoil at $\alpha = 22^\circ$. (lower graph is expansion of leading edge region)

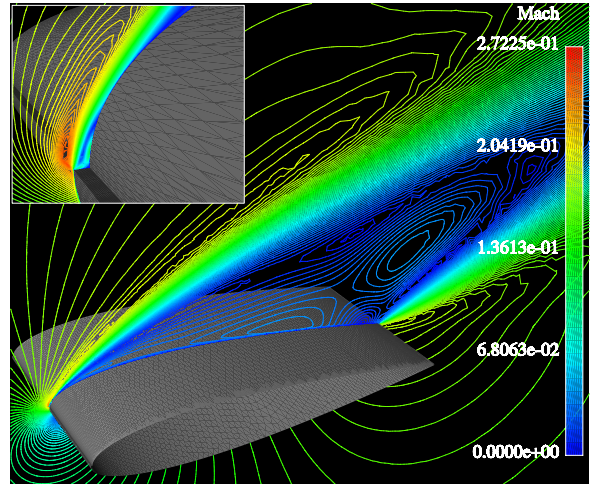


Figure 19: Mach contour map at centerline cut for TAU0015 airfoil at $\alpha = 22^\circ$ (insert of leading edge region).

uments a comparison of computational results using the baseline airfoil (no control) with experimental data.

The two-dimensional results show that the mid-chord discontinuity is insignificant and can be faired over for more efficient computational studies. The leading-edge discontinuity significantly affects the lift and drag; hence, the integrity of the leading-edge notch discontinuity must be maintained in the computations to achieve a good match with the experimental data. The pressure coefficients match the experimental data in all cases except for the highly stalled conditions. The comparison of computed lift and drag coefficients with angle-of-attack is in extremely good agreement with wind-tunnel data when the computational and experimental methods of computing the coefficients are the same.

For all conditions, the three-dimensional pressures were slightly overpredicted in comparison with the two-dimensional and experimental data. The greatest overprediction occurred near the leading-edge of the airfoil. The three-dimensional, computational lift versus angle-of-attack results match the experiments in the pre-stall region ($\alpha \simeq 10^\circ$) and the drag coefficient matches the experiments in post-stall conditions ($\alpha > 12^\circ$). For the near-stall and post-stall regions, the computational results deviate from the experimental results, with a lower calculated C_l probably due to either lack of grid resolution or side-wall interference. The three-dimensional results show a spanwise bias to the separation on both sides of the airfoil centerline; as yet

this bias is not completely understood.

Future research will focus on refining the three-dimensional grid to more fully capture the baseline (no control) aerodynamics. The impact of far-field boundary locations will be assessed for separated flows relative to predicted performance. The current study will be extended to include RANS validation of unsteady vortex shedding problems. Finally, actuator boundary condition models will be introduced to attempt the validation of unstructured-grid RANS for active flow control.

7 Acknowledgments

The authors are indebted to Dr. Avi Seifert, Tel-Avi University, for the insightful discussion of flow control and for supplying the geometry and experimental data for the TAU0015 model. Also, we are grateful for the use of Dr. W. Kyle Anderson's FUN2D and FUN3D codes.

8 References

- ¹Gad-el-Hak, M., "Flow Control," *Applied Mechanics Review*, Vol. 42, No. 10, 1989, pp. 261-293.
- ²Gad-el-Hak, M., and Bushnell, D. M., "Separation Control: Review," *J. Fluids Engineering*, Vol. 113, 1991, pp. 5-30.
- ³Chang, P. K. *Control of Flow Separation: Energy Conservation, Operational Efficiency, and Safety*. Hemisphere Publishing Corp., Washington D.C., 1976.
- ⁴Lin, J. C., "Control of Turbulent Boundary-Layer Separation using Micro-Vortex Generators," AIAA Paper 99-3404, June 1999.
- ⁵Joslin, R. D., "Overview of Laminar Flow Control," *NASA/TP-1998-208705*, October 1998.
- ⁶McLean, J. D., Crouch, J. D., Stoner, R. C., Sakurai, S., Seidel, G. E., Feifel, W. M., and Rush, H. M., "Study of the Application of Separation Control by Unsteady Excitation to Civil Transport Aircraft," *NASA/CR-1999-209338*, June 1999.
- ⁷Chandrasekhara, M. S., Wilder, M. C., and Carr, L. W., "Control of Flow Separation Using Adaptive Airfoils," AIAA Paper 97-0655, January 1997.
- ⁸Seifert, A., Bachar, T., Wygnanski, I., Kariv, A., Cohen, H., and Yoeli, R., "Application of Active Separation Control to a Small Unmanned Air Vehicle," *Journal of Aircraft*, Vol. 36, No. 2, 1998, pp. 474-477.
- ⁹Seifert, A., Eliahu, S., Greenblatt, D., and Wygnanski, I., "Use of Piezoelectric Actuators for Airfoil Separation Control," *AIAA Journal*, Vol. 36, No. 8, 1998, pp. 1535-1537.
- ¹⁰McManus, K. and Magill, J., "Separation Control in Incompressible and Compressible Flows using Pulsed Jets," AIAA Paper 96-1948, June 1996.
- ¹¹Seifert, A., Darabi, A., and Wygnanski, I., "Delay of Airfoil Stall by Periodic Excitation," *Journal of Aircraft*, Vol. 33, No. 4, July-August 1996, pp. 691-698.
- ¹²Seifert, A. and Pack, L. G., "Oscillatory Excitation of Unsteady Compressible Flows over Airfoils at Flight Reynolds Numbers," AIAA Paper 99-0925, January 1999.
- ¹³Seifert, A. and Pack, L. G., "Oscillatory Control of Separation at High Reynolds Numbers," *AIAA Journal*, Vol. 37, No. 9, 1999, pp. 1062-1071.
- ¹⁴Pack, L. G. and Seifert, A., "Periodic Excitation for Jet Vectoring and Enhanced Spreading," AIAA Paper 99-0672, January 1999.
- ¹⁵Kral, L. D., Donovan, J. F., Cain, A. B., and Cary, A. W., "Numerical Simulation of Synthetic Jet Actuators," AIAA Paper 97-1824, June 1997.
- ¹⁶Donovan, J. F., Kral, J. D., and Cary, A. W., "Active Flow Control Applied to an Airfoil," AIAA Paper 98-0210, January 1998.
- ¹⁷Ravindran, S. S., "Active Control of Flow Separation over an Airfoil," *NASA/TM-1999-209838*, December 1999.
- ¹⁸Wu, J.-Z., Lu, X.-Y., Denny, A. G., Fan, M., and Wu, J.-M., "Post-Stall Flow Control on an Airfoil by Local Unsteady Forcing," *Journal of Fluid Mechanics*, Vol. 371, 1998, pp. 21-58.

- ¹⁹ Seifert, A. (personal communication), November 2000.
- ²⁰ Anderson, W. K. and Bonhaus, D. L., "An Implicit Upwind Algorithm for Computing Turbulent Flows on Unstructured Grids," *Computers Fluids*, Vol. 23, No. 1, 1994, pp. 1-21.
- ²¹ Anderson, W. K., Rausch, R. D., and Bonhaus, D. L., "Implicit/Multigrid Algorithms for Incompressible Turbulent Flows on Unstructured Grids," *Journal of Computational Physics*, Vol. 128, 1996, pp. 391-408.
- ²² Spalart, P. R., and Allmaras, S. R., "A One-Equation Turbulence Model for Aerodynamic Flows," AIAA Paper 92-0439, January 1992.
- ²³ Marcum, D. L., "Generation of Unstructured Grids for Viscous Flow Applications," AIAA paper 95-0212, Jan. 1995.
- ²⁴ Marcum, D. L., and Weatherhill, N. P., "Unstructured Grid Generation Using Iterative Point Insertion and Local Reconnection," *AIAA Journal*, Vol. 33, No 9, September 1995, pp. 1619-1625.
- ²⁵ Pirzadeh, S., "Structured Background Grids for Generation of Unstructured Grids by Advancing-Front Method," *AIAA Journal*, Vol. 31, No 2, February 1993, 257-265.
- ²⁶ Pirzadeh, S., "Progress Toward A User-Oriented Unstructured Viscous Grid Generator," AIAA-96-0031, Jan. 1996.
- ²⁷ Pirzadeh, S., "Three-Dimensional Unstructured Viscous Grids by the Advancing-Layers Method," *AIAA Journal*, Vol. 34, No 1, January 1996, pp. 43-49.
- ²⁸ McCroskey, W. J., McAlister, K. W., Carr, L. W., and Pucci, S. L., "An Experimental Study of Dynamic Stall on Advanced Airfoil Sections Volume 1. Summary of the Experiment," *NASA Technical Memorandum 84245*, July 1982.
- ²⁹ McCroskey, W. J., "A Critical Assessment of Wind Tunnel Results for the NACA 0012 Airfoil," *AGARD CP 429*, 1987.